Available online at www.sciencedirect.com
SCIENCE DIRECT®
International Journal of Heat and Mass Transfer 47 (2004) 4869–4879
International Journal of HEAT and MASS TRANSFER
www.elsevier.com/locate/ijhmt

Numerical simulation of laminar and turbulent buoyancy-driven flows using a lattice Boltzmann based algorithm

Y. Zhou *, R. Zhang, I. Staroselsky, H. Chen

Exa Corporation, 450 Bedford Street, Lexington, MA 02420, USA

Received 4 December 2003; received in revised form 15 April 2004
Available online 24 July 2004

Abstract

The capability of simulating natural and forced convection has been recently developed and integrated into PowerFLOW, a general purpose CFD solver based on the lattice Boltzmann algorithm. Several benchmark tests have been performed to validate this buoyancy model. Two typical cases of Rayleigh–Bénard convection with the Rayleigh number slightly above ($Ra = 2000$) and below ($Ra = 1500$) the critical Rayleigh number of 1708 were tested to verify the conceptual and algorithmic correctness of the buoyancy model. Then simulations of turbulent natural convection in an enclosed tall cavity with two different Rayleigh numbers, $Ra = 0.86 \times 10^6$ and $Ra = 1.43 \times 10^6$, were carried out and found to be in a very good agreement with the experiments of Betts and Bokhari.

Keywords: Lattice Boltzmann; Buoyancy; Natural convection; CFD

1. Introduction

Natural convection, or buoyant force driven flow due to temperature differences in the fluid is one of the classical hydrodynamic topics that span off seminal research in stability theory, dynamical systems, and nonlinear science in general [1]. In addition to this fundamental importance, buoyancy effects are essential in a variety of industrial applications involving significant spatial variation of temperature, such as in solar energy collectors, building ventilation, chimney design, automotive under-hood flows, boiler design, etc. Also, in meteorological flows the buoyancy force is almost always important.

Except for the simplest geometries and slightly supercritical regimes, no analytical solutions exist for buoyant flows. With the help of computers, the equations governing convective flows can now be solved numerically. These simulations are of course limited by the power of both computers and the numerical algorithms employed. Currently, direct numerical simulation (DNS) is limited to low Reynolds number situations whereas for high Reynolds number flows turbulence modeling becomes necessary. When applied to natural convection, the entire turbulence modeling approach involves specific as well as non-specific difficulties. First of all, an accurate boundary layer model is necessary to treat wall-bounded flows unless the viscous sublayer can be resolved, which is practically impossible at high Reynolds number [2–4]. However, no such universally valid model exists at the present time. In addition, the Reynolds numbers for buoyancy-driven turbulence are often in the transitional range, which makes the modeling issues even harder. Furthermore, the presence of buoyancy force introduces an additional anisotropy of the unresolved scales and thus invalidates some of the assumptions intrinsic in traditional turbulence closures, especially the two-equation turbulence models.

* Corresponding author. Tel.: +781-676-8500; fax: +781-676-8599.
E-mail address: zhou@exa.com (Y. Zhou).

0017-9310/$ - see front matter © 2004 Published by Elsevier Ltd.
doi:10.1016/j.ijheatmasstransfer.2004.05.020

As early as in 1993, researchers started to directly simulate Rayleigh–Bénard convection using lattice Boltzmann-based approach [5–7]. Since then, the lattice Boltzmann-based numerical algorithm has been significantly improved over the past 10 years or so. The instability of Rayleigh–Bénard convection near the critical Rayleigh number can be accurately predicted by LBM approach [8].

In this paper, we demonstrate that combining lattice Boltzmann method (LBM) with turbulence modeling in an all-purpose code can simulate difficult natural convection flows with very good accuracy. Since the last decade, LBM has developed as an important alternative to conventional computational fluid dynamics (CFD) methods. Based on microscopic kinetic theory, LBM uses a simple kinetic model obeying fundamental conservation laws and symmetries in order to simulate macroscopic hydrodynamics. It is well recognized that at the nearly incompressible limit LBM is essentially an explicit finite-difference scheme with the second order accuracy in both time and space [9,10]. Many physical models and extensions of the method have been formulated that cover a wide range of complex fluids and flows. Because of its many desirable features such as low numerical diffusion, scalable performance in parallel computing environment, coding simplicity, and robustness in dealing with complex boundary conditions, LBM has already had substantial impact on fundamental research and engineering applications [10–17].

PowerFLOW is a general purpose CFD solver for turbulent and laminar weakly compressible flow based on lattice Boltzmann algorithms. In addition to the common advantages of LBM that are listed above, it has several key extensions to the basic LBM algorithm:

(a) An advanced renormalized group theory (RNG) based turbulence model is incorporated into the basic LBM. In addition to providing LBM with the general capability to model high Reynolds number flow, RNG model is well suited for performing time-dependent very large eddy simulations (VLES) [18–21]. Implementation of the turbulence modeling capability has been only possible on the foundation of a unique slip algorithm that relates particle distribution functions at a solid wall to the microscopically defined local value of wall shear stress.
(b) An additional scalar transport equation coupled with LBM is introduced for predicting temperature evolution. By removing the energy conservation constraints in LBE, the numerical stability and solver's capability are greatly improved [22,23].
(c) A volumetric based surface scatter algorithm is applied for accurate calculation of the surface mass and momentum fluxes in general flow/geometry situations [24].

During the last few years, many academic and industrial benchmarks have been successfully validated against experimental data. Lattice Boltzmann method now plays an increasingly important role in engineering research and applications [25–27].

In this paper, we first describe some of the fundamental LBM extensions for buoyancy, heat transfer and turbulence. These form the core algorithms. Then we present benchmark simulations of buoyancy-driven flows. The two-dimensional Rayleigh–Bénard convection and turbulent natural convection in an enclosed tall cavity have been simulated to verify and validate the solver. Although LBM has been used in direct numerical simulation of Rayleigh–Bénard convection in the past [5–8,28], this is the first application of turbulence modeling approach combined with lattice Boltzmann methodology to simulate turbulent convection and especially to study quantitative details of turbulent boundary layer. Conclusions are drawn at the end based on these simulation results.

2. The numerical algorithm

2.1. Extended lattice Boltzmann method

The most common form of the lattice Boltzmann equation (LBE) is [10,13,29]:

$$f_i(\mathbf{x} + \hat{c}_i\Delta t, t + \Delta t) - f_i(\mathbf{x}, t) = C_i, \tag{1}$$

where f_i are the particle density distributions defined for the finite set of discrete particle velocity vectors $\{\hat{c}_i: i = 0, \ldots, b\}$. These particle speeds define links among nodes on a given lattice. The collision term on the right-hand side of Eq. (1) now often uses the so called Bhatnagar–Gross–Krook (BGK) approximation [13,14,17,29],

$$C_i = -\frac{f_i - f_i^{\mathrm{eq}}}{\tau}, \tag{2}$$

with a single relaxation time τ. Here, f_i^{eq} is the local equilibrium distribution function that has an appropriately prescribed functional dependence on the local hydrodynamic properties. The basic hydrodynamic quantities, such as fluid density ρ and velocity $\mathbf{u}$, are obtained through moment summations in the velocity space

$$\begin{aligned} \rho(\mathbf{x}, t) &= \sum_i f_i(\mathbf{x}, t), \\ \rho\mathbf{u}(\mathbf{x}, t) &= \sum_i \hat{c}_i f_i(\mathbf{x}, t). \end{aligned} \tag{3}$$

In addition, one can also define a fluid temperature T from

$$\rho\frac{D}{2}\ T(\mathbf{x},t)=\sum_i\frac{1}{2}\ (\hat{c}_i-\mathbf{u}(\mathbf{x},t))^2 f_i(\mathbf{x},t), \tag{4}$$

where D is the dimension of the momentum space defined by the set of discrete lattice velocities [30]. With an appropriate choice of lattices and suitable f_i^{eq}, the LBE obeys conservation laws for mass, momentum, and energy in the physical space and recovers the Navier–Stokes equations at a long wavelength, low frequency limit through a Chapman–Enskog expansion [10]. The ideal gas equation of state, $p=\rho T$, is also recovered. The fluid kinematic viscosity is uniquely mapped to the relaxation time:

$$v=\left(\tau-\frac{1}{2}\right)T, \tag{5}$$

including situations where both v and τ vary non-trivially in time/space as defined by complex physics phenomena that are not necessarily reducible to directly modeled hydrodynamics [17].

With the conserved energy degree of freedom, the common LBM can be naturally extended to simulate thermodynamics [10,15,31]. When a sufficient number of particle speeds is used, it can be shown theoretically that the LBM leads to the correct full set of thermohydrodynamic equations of an ideal-gas fluid [15,31]. However, from both the fundamental and practical points of view such an approach has several drawbacks. First of all, it has been proven that LBMs with the energy degree of freedom do not automatically guarantee the global H-theorem [22,32]. As a consequence, each such system is potentially more unstable than the corresponding non-energy-conserving scheme. Second, without a substantial generalization to the BGK collision term it is difficult to achieve Prandtl number values that are substantially different from unity. Also, the temperature range is limited in such a way that the maximal allowable value of temperature achieved in the thermal lattice Boltzmann approach is only about twice the minimal value. Finally, there are significant compressibility effects in body force related thermal flows.

To overcome these issues, in this work we drop the constraint of energy conservation in the LBM and introduce an additional scalar transport equation for the energy evolution [23]. It should be mentioned that the same approach is currently used for all thermal transport related problems in our work. The fundamental idea of this LBM based algorithm can be briefly summarized as follows. First of all, the fluid dynamics part (i.e., the mass and momentum evolution) is represented by a modified isothermal LBM, while the energy evolution part is determined by an additional transport equation [8,28,6]. The latter can be solved via either a finite difference scheme or an auxiliary LBM. Secondly, these two parts are coupled through a properly defined buoyancy force term in the LB module of the solver. Because of the absence of temperature dynamics in the equilibrium distribution functions, this LBM based thermal scheme can achieve much improved numerical stability while still recovering the same macroscopic thermodynamics. The supplemental energy transport equation has the usual form:

$$\rho C_p(\partial_t+\mathbf{u}\cdot\nabla)T=\nabla\cdot\kappa\nabla T+\Psi, \tag{6}$$

where $\kappa=\rho C_p v/Pr$ is the heat conductivity that can be specified flexibly according to the desired Prandtl number. The Ψ-term represents viscous dissipation as well as the other volumetric energy sources. The limitations on the Prandtl number and temperature variation range are no longer present in this approach. Solving the scalar transport equation is a rather straightforward computational task. In our simulations, an extended Lax-Wendroff scheme is applied [16,20].

Under the Boussinesq approximation, the buoyancy force can be calculated in a straightforward way based on the temperature field variation

$$\mathbf{F}_b(\mathbf{x},t)=\rho(\mathbf{x},t)\cdot\mathbf{g}\cdot\alpha\cdot(T(\mathbf{x},t)-T_{\mathrm{ref}}), \tag{7}$$

where $\mathbf{g}$ is the gravity acceleration, T_{ref} is a constant reference temperature, and $\alpha=-\frac{1}{\rho}(\frac{\partial\rho}{\partial T})_p$ is the thermal expansion coefficient. Ignoring higher order contributions in the local Knudsen number, the appropriate buoyancy force that needs to be fed back into the LBM can be simply expressed as [33]

$$\Delta f_i(\mathbf{x},t)=\frac{w_i}{\rho T_0}\hat{c}_i\cdot\mathbf{F}_b(\mathbf{x},t), \tag{8}$$

where the constant weights w_i and T_0 are directly determined by the particular LBE model used for the corresponding non-buoyant case. It is easy to show that at each time step the local momentum is altered by the following amount:

$$\mathbf{F}_b(\mathbf{x},t)=\sum_i\hat{c}_i\Delta f_i(\mathbf{x},t). \tag{9}$$

The combination of Eqs. (1)–(3), (6)–(8) forms our hybrid LBM scheme for modeling buoyant flow.

2.2. Fluid turbulence model

In our current simulations of high Reynolds number flow, the subgrid scale effect of turbulence on the resolved flow field is through eddy viscosity v_t and turbulent thermal diffusivity χ_t ($=v_t/Pr_t$). A two-equation model based on the Renormalized Group (RNG) turbulence model [18,19] is applied to determine the turbulent transport coefficients

$$\frac{\partial k}{\partial t}+\mathbf{u}\cdot\nabla k=\nabla\cdot\left[\left(\frac{v_0}{\sigma_{k0}}+\frac{v_e}{\sigma_{ke}}\right)\nabla k\right]+v_e|S|^2-\epsilon$$
$$\frac{\partial \epsilon}{\partial t}+\mathbf{u}\cdot\nabla \epsilon=\nabla\cdot\left[\left(\frac{v_0}{\sigma_{\epsilon 0}}+\frac{v_e}{\sigma_{\epsilon e}}\right)\nabla \epsilon\right]+C_{\epsilon 1}v_e\frac{\epsilon}{k}|S|^2-\left[C_{\epsilon 2}+C_\mu\frac{\tilde{\eta}^3(1-\tilde{\eta}/\eta_0)}{1+\beta\tilde{\eta}^3}\right]\frac{\epsilon^2}{k}. \quad (10)$$

Here, $|S|$ is the magnitude of the strain rate tensor of the resolvable velocity field, and $\tilde{\eta}$ is a function of $\eta(\equiv k|S|/\epsilon)$, η_ω $(\equiv k|\Omega|/\epsilon)$ and local helicity, as a generalization from [18,19]. Similar to the scalar energy transport equation, the above equations are solved on the same lattice with an extended Lax–Wendroff scheme [20].

2.3. Boundary conditions

In this work, we use the volumetric scattering based boundary condition treatment as the general scheme [24]. For both basic research and real-world engineering applications, this approach has a number of advantages over the point-wise bounce back algorithm often used in the academic community. First, it ensures exact conservation of surface fluxes of mass, momentum, and even energy on the discretized surface facets, which is critical to the realization of turbulent wall functions. Also, it allows for smooth surface distribution of physical quantities. Finally, this algorithm is capable of dealing with arbitrary complex geometries.

Here we briefly outline the basic concept of this approach. On a facetized surface in Fig. 1, each facet has a set of extruded parallelogram (parallelepiped in three dimensions) corresponding to the discrete directions ($\mathbf{c}_i$) with the volumes, $V_i^\alpha=|\mathbf{c}_i\cdot\mathbf{n}^\alpha|A^\alpha\Delta t$. $\mathbf{n}$ is a surface normal of the facet pointing towards the fluid domain side, and A^α is the surface area of the facet. At each time step, the advection process propagates particles from the overlapping area of each fluid cell and parallelogram of each facet to the facet along the particle moving directions. Then on each facet, momentum flux is treated according to different boundary types. For the no-slip type, the particle momentum is reversed in both the normal and tangential directions. For the free-slip type, the particle momentum is reversed in the normal direction while still maintained in the tangential direction. The zero mass flux is always maintained [24]. Precise control of the tangential momentum flux, via a proper combination of the no-slip and free-slip conditions, is the key to achieve correct turbulent momentum flux based on a momentum wall function. For this study, the following wall function is applied

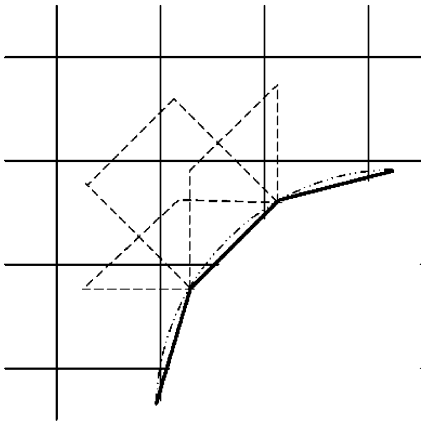

Fig. 1. Illustration of volumetric boundary condition. The dark-solid line segments are facets of the curved surface (dash-dotted line), the dashed-line-bounded regions represent parallelograms in particle moving directions.

$$u_+=2.44\ln y_+ + 5.5,$$

where $u_+=u/u_*$ and $y_+=y*u_*/v$. Here u_* is the surface friction velocity, and y the normal distance from the wall. A thermal wall function based on standard similarity laws [1] is also used for predicting temperature in turbulent boundary layers.

$$T_+=1.75\ln y_+ + 3.9,$$

where $T_+=(T_\mathrm{w}-T)\rho C_p u_*/q_\mathrm{w}$. Here T_w is the surface temperature and q_w the surface heat flux. This thermal wall function relates near wall fluid temperature values evolving according to Eq. (6) to the fixed values of surface temperature and/or heat flux, using the microscopically defined wall shear stress and macroscopically defined turbulent quantities. In this way, both the Von Neumann and Dirichlet problems for Eq. (6) are well posed.

Multiple variable resolution regions (VRs) are applied in the simulations. The resolution differs by a factor of two between VRs that are next to each other. On the VR boundaries, all quantities, including the particle distribution functions, turbulent properties, fluid temperature, etc, are treated in such a way that conservation of mass, momentum and energy is preserved and the mean flow as well as turbulent quantities are continuous across the interface.

3. Simulation results

3.1. Rayleigh–Bénard convection

Rayleigh–Bénard convection has been extensively studied theoretically, experimentally, and numerically. We have simulated several near-critical situations in order to conceptually verify the buoyancy model. We concentrate on one of the most common setups of

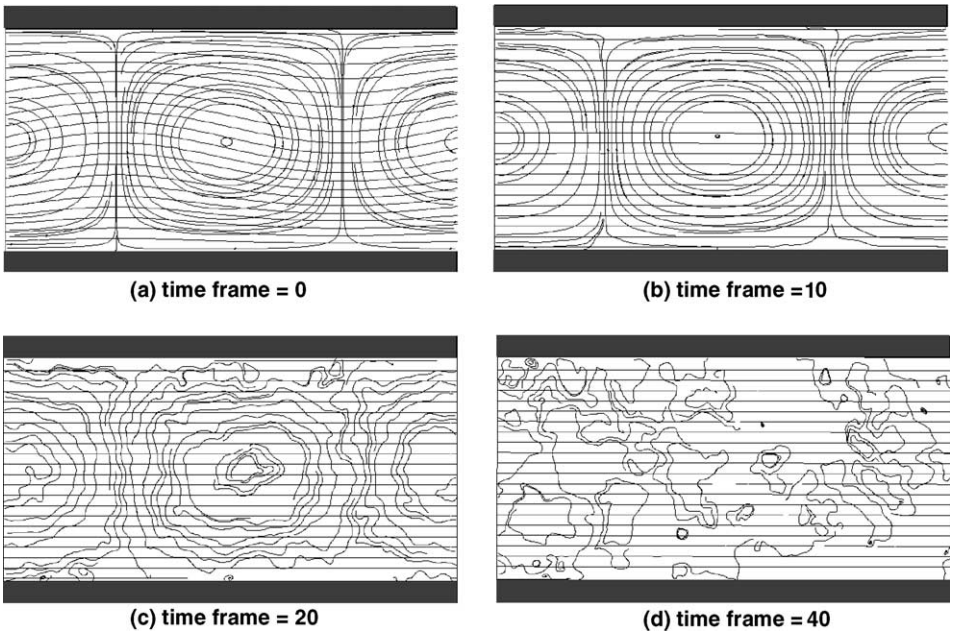

Fig. 2. Case I: isotherms and flow streamlines at $Ra = 1500$.

Rayleigh–Bénard convection, where a thin layer of viscous fluid is confined by two horizontal rigid plates maintained at different temperatures (Fig. 2). The net buoyancy force acting on fluid with a positive thermal expansion coefficient is in the opposite direction to the gravity. Therefore, there is a net upward buoyancy force acting on the fluid if the bottom plate is maintained at a higher temperature than the top one. The classical studies tell us that at a small temperature difference, the buoyancy force is balanced by viscous drag and heat diffusion. The fluid will remain quiescent until the temperature difference exceeds a certain critical value, after which the still fluid becomes unstable and convective motion occurs.

The ratio of buoyancy force to the product of viscous force and heat diffusion rate defines the Rayleigh number

$$Ra \equiv \alpha \Delta T \frac{gL^3}{\nu\chi}, \tag{11}$$

where α is the thermal expansion coefficient, T_h and T_c are the temperatures of the hot, lower and the cold, upper plates, respectively, $\Delta T = T_h - T_c$, g is the magnitude of gravitational acceleration, L is the distance between the plates, ν is the kinematic viscosity, and $\chi = \kappa/\rho C_p$ is the thermal diffusivity. Convection occurs when the Rayleigh number exceeds a critical value Ra_c. There is a classical theoretical result, well confirmed by both experiment and numerical simulation, that the critical Rayleigh number for the configuration shown in Fig. 2 is $Ra_c = 1708$, above which the fluid become unstable and two dimensional rolls form if the deviation from the Boussinesq approximation is small. For verification of the basic algorithm, we use the fact that the instability develops very slowly at near-critical Rayleigh numbers and that the first unstable disturbance is two dimensional. Therefore, performing all the tests in 2D should save computational time without sacrificing accuracy.

As mentioned above, LBM-based simulation of slightly supercritical convection has been already reported by Shan [8], whose 2D setup we exactly follow. The x-axis is attached on the cold wall pointing to the right and the y-axis points down towards the hot wall. The coordinate origin is fixed at the upper left corner. Periodic boundary conditions are applied in the x-direction and non-slip boundary conditions are applied at the rigid walls. The aspect ratio L_x/L_y is chosen to be commensurate with $2\pi/k_c$, where L_x is the plates' length, L_y is the distance between the plates, and $k_c = 3.12$ is the analytically known non-dimensional wave number of the first unstable mode. The resolution is therefore chosen as 101 lattice cells in the x-direction and 50 lattice cells in the y-direction. Gravitational acceleration is along the y-direction.

Two cases with different Rayleigh numbers have been set up to test the model near the critical Rayleigh number. In Case I, the Rayleigh number is 1500 so that the fluid should stay stationary. In Case II, the Rayleigh number equals 2000 so that one should expect supercritical behavior and pattern formation.

3.1.1. Case I: Ra = 1500

It could be very difficult to observe whether or not the initially still fluid will remain stationary at slightly sub-critical Rayleigh number since the instability (if any) would develop very slowly. In contrast, it is much easier to detect whether an initially non-uniform flow eventually becomes stationary under the same conditions. Therefore, to test whether at $Ra = 1500$ the fluid becomes asymptotically stationary an initial large perturbation was applied to the temperature field:

$$T_0 = T_c + \frac{y}{L_y}\Delta T\left(0.8 + 0.2\sin\left(2\pi\frac{x}{L_x}\right)\right). \tag{12}$$

The simulation was started from zero fluid velocity.

This case was simulated on a Linux machine with a single 2.4 GHz CPU. It took about 1.5 h to reach 120,000 timesteps, or 4.3×10^{-6} s per timestep per voxel.

It is observed that under this perturbation, the fluid is unsteady initially. Two convective cells can be seen in Fig. 2(a) and (b). With time, this artificially induced convection dies out and the cells gradually disappear, as seen in Fig. 2(c) and (d). Fig. 2 also shows that the temperature field was disturbed initially, but gradually became linear as the flow turned into the purely conductive state. This simulation has run for 120,000 timesteps to make sure the fluid remains stationary thereafter. Reaching a stationary regime is further demonstrated in Fig. 4(a) where we plot the vertical velocity at a fixed point as a function of time. The measurement point was chosen at a place where the maximum value was expected corresponding to the existence of two convective cells at the initial time. The magnitude of vertical velocity decreases as the convective cells are weakening over time until it finally drops to the random noise level when the cells disappear around the time frame 20 (equivalent to 60,000 timesteps). The vertical velocity is always positive when a pronounced cell pattern can be observed as shown in Fig. 2(a) and (b). However, after frame 20, no clear flow pattern may be seen as shown in Fig. 2(c) and (d). The vertical velocity is actually fluctuating around zero after frame 20 as shown in Fig. 4(a), which confirms that the flow has become stationary.

3.1.2. Case II: Ra = 2000

Here we expect the instability to develop naturally, so the simulation was started from the purely conductive static state. No perturbation was introduced except for the intrinsic machine noise. It was simulated on the same Linux box mentioned above and took about 2.7 h (210,000 timesteps) to reach quasisteady-state.

Shown in Fig. 3 are isotherms and flow streamlines at different time instants. Initially, the temperature is distributed linearly in the vertical direction (Fig. 3a). After about 100,000 timesteps (or 20 time frames), two convective cells start to form (Fig. 3b), although the average velocity magnitudes are small compared to that at the final stable convective state (see Fig. 4b). The temperature field is slightly disturbed at this stage. The flow continues to develop into stronger convective cells until

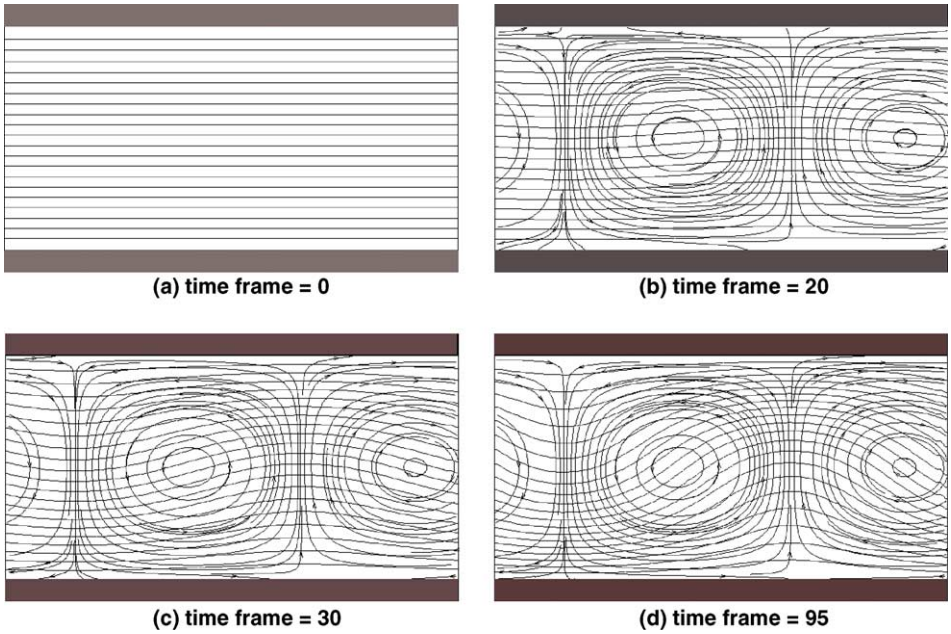

Fig. 3. Case II: flow isotherms and streamlines at $Ra = 2000$.

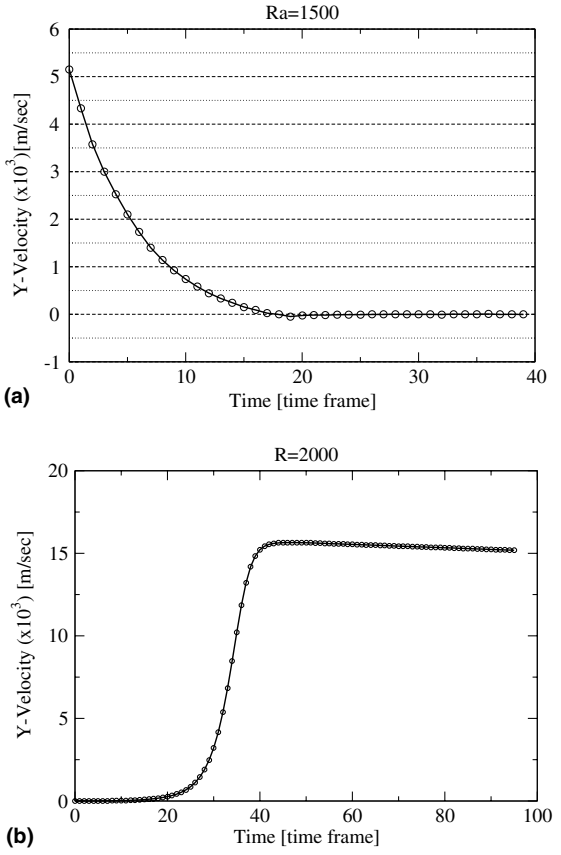

Fig. 4. Vertical velocity as a function of time: (a) the data were recorderd every 3000 timesteps (1 time frame) and (b) 5221 timesteps (1 time frame).

it reaches a stable quasisteady-state (Fig. 3c and d). The simulation was stopped at half a million timesteps.

As the elegant physics of near-critical convective cells has been extensively studied before, all of our results presented above should be viewed as just a verification of the hybrid LBM/macroscopic approach applied to buoyancy in the code. In this regard, let us reiterate that there has been much previous DNS work on this problem, including the LBM-based study of [8]. Our results are perhaps much more novel for the difficult problem of high Rayleigh number, turbulent convection to which we now turn.

3.2. Turbulent natural convection in an enclosed tall cavity

Turbulent natural convection in a confined enclosure with two differentially heated vertical walls has been and remains to be an attractive and challenging subject in turbulence research [34–36]. In this configuration, buoyancy is the only driving force for fluid motion, but it does not make the problem any simpler. As a matter of fact, although much of the flow is turbulent, there are extensive low Reynolds number regions and even regions of laminar flow, which poses a significant challenge to near-wall turbulence modeling. Note that in vertical convective cell boundary layers the shear stress varies rapidly and changes sign whereas the near-wall heat flux is about constant. Aside from being interesting from the modeling point of view, this setup carries a number of features important for industrial applications involving natural convection within enclosures, such as electronic device cooling, building ventilation, solar energy collectors, and many others.

Despite this fundamental and practical importance, high quality experimental data on turbulent natural convection in enclosures including both temperature and velocity fields is quite limited [36–38]. The experiment of Betts and Bokhari [36] might be the only one that has easily accessible public data at http://cfd.me.umist.ac.uk/ercoftac/ (case 79).

The experimental data is available for a rectangular, large aspect ratio (2.18 m high by 0.076 m wide by 0.52 m deep), air-filled cavity. From the point of view of turbulence model verification studies, there are advantages for choosing a high aspect ratio cavity versus near-square cavity. The cavity width-based Rayleigh number that is required to ensure turbulent flow within the cavity is much smaller than that for a square cavity. This means that the cavity width and/or the temperature difference can be made smaller. The reduced temperature difference between the vertical walls makes it possible to neglect the air molecular property variation within the cavity.

In the experiment [36], two different Rayleigh numbers of 0.86×10^6 and 1.43×10^6 were achieved by varying the temperature difference between vertical plates. Under these conditions the cavity core flow is fully turbulent and the air property variations with temperature are small (see Table 1). The temperature and flow patterns were found to be closely two-dimensional.

In our studies, two simulation cases were set up after the above mentioned experimental conditions, but reduced to two dimensions (Fig. 5). The cold and hot walls have fixed temperatures listed in Table 2. The horizontal variation of surface temperature at the top and bottom

Table 1
Properties of dry air

Temperature (°C)	15.1	34.7	54.7
Thermal conductivity (W/m K × 10^3)	25.3	26.8	28.3
α ($K^{-1} \times 10^3$)	3.47	3.25	3.05
ν ($m^2/s \times 10^6$)	14.6	16.5	18.4
Prandtl number	0.704	0.700	0.697

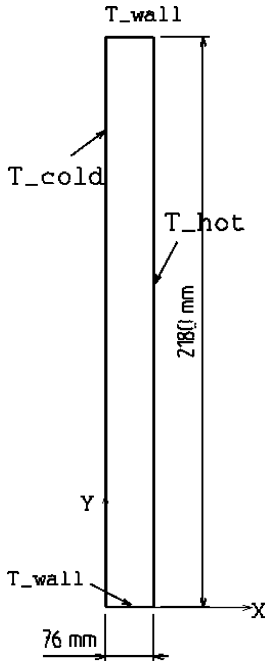

Fig. 5. Sketch of the 2D tall cavity.

Table 2
Parameters for the two Rayleigh numbers

Rayleigh number	0.86×10^6	1.43×10^6
Cold wall temperature (°C)	15.1	15.6
Hot wall temperature (°C)	34.7	54.7

walls was not exactly linear in the experiment, but to simplify the computational case setup we use a linear fit

$$T_{\text{wall}} = T_{\text{c}} + \frac{x}{W}(T_{\text{h}} - T_{\text{c}}),$$

where T_{wall} is the temperature of the top or bottom wall, T_{c} (T_{h}) is the cold (hot) wall temperature, x is the distance from the cold wall, and W is the cavity width. Turbulent wall boundary conditions, as discussed in Section 2.3, are applied to all solid surfaces that enclose this cavity.

The fluid is initialized with zero velocity and linear temperature profile set by T_{wall}. A resolution dependence study has been performed, with the special emphasis paid to the sensitivity of the simulation results to resolving the large temperature gradients near vertical walls. Shown in Fig. 6 are temperature profiles at the middle-height ($y/H = 0.5$) obtained with three different resolutions. The first set of data corresponds to a resolution of 50 lattice cells across the cavity width (the solid line), denoted by h50. The data obtained using the h100 resolution is plotted with the dashed line and h150 with dot-dashed line. Also shown in Fig. 6 are the experimental data. It is clear that there is virtually no difference between higher resolution (h100 and h150) results which agree with the experiment very well, but using lower resolution leads to a significant under-prediction of the temperature slope.

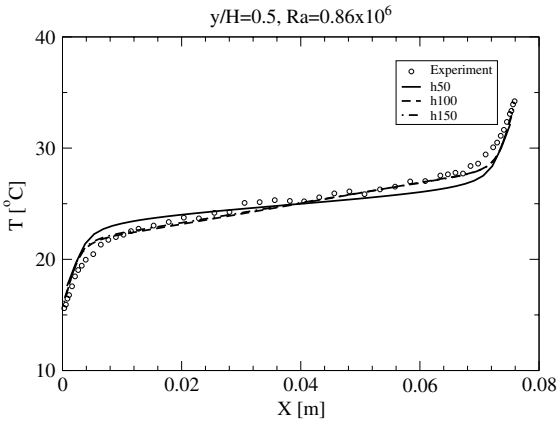

Fig. 6. Simulation results with three different resolutions of h50, h100, and h150.

However, it is only natural to assume that such a high resolution may be unnecessary in the regions away from the vertical walls where the temperature gradients are small, in full analogy with the conventional CFD

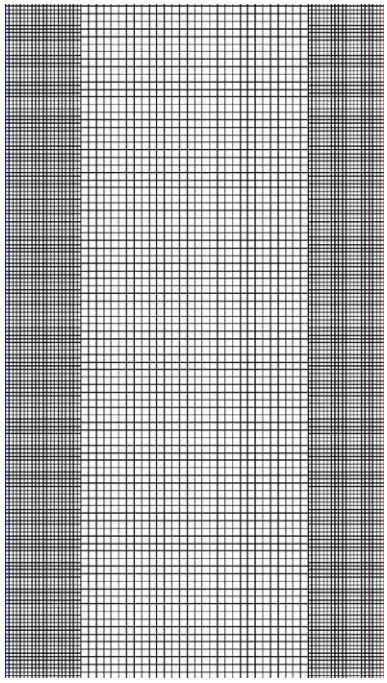

Fig. 7. Lattice grids used in the resolution dependence study. The near-wall resolution is doubled.

wisdom. A case was set up in order to examine whether the higher resolution is only needed near the vertical walls (Fig. 7). In this case, the resolution at the center region is h50 but is doubled in the near wall regions. Compared to the uniform resolution case of h100, the results are virtually the same. Therefore, this variable resolution was used for all the simulations thereafter.

The simulation was performed on a Compaq AlphaServer ES40 with 4500 MHz CPUs. It took about 11 h to reach equilibrium state, or 2×10^{-5} s per timestep per voxel. Shown in Figs. 8 and 9 are the mean temperature profiles at various heights for $Ra = 0.86 \times 10^6$ and $Ra = 1.43 \times 10^6$, respectively. The solid lines correspond to the simulation results and the circles represent experimental data. In both cases, the predicted mean temperature profiles agree with experimental data very well. The mean vertical velocity profiles predicted by the numerical simulations also agree with the experiment well in general. The discrepancy between the simulation results and the experiment becomes larger in the regions close to the top and bottom walls (not shown in the plots) where the deviation of the computational setup from the experimentally imposed/observed boundary conditions plays a stronger role.

We have been unable to find any published CFD results related to this configuration, although it has been used as one of the test cases for the 5th ERCOFTAC/IAHR Workshop on Refined Flow Modelling in 1996 [36]. The simulation results shown in Figs. 8 and 9 are considered to be very satisfactory. However, there is still room to improve their quality. As but one example, the temperature boundary conditions at the top and bottom walls may be refined by interpolating the near-surface experimental data. Let us also emphasize that these data have been obtained with an all-purpose software that contains no adjustable parameters specific to the convective flow setups studied here. As such, these results may attest not only to the correctness of the buoyancy model implementation but to the general quality of

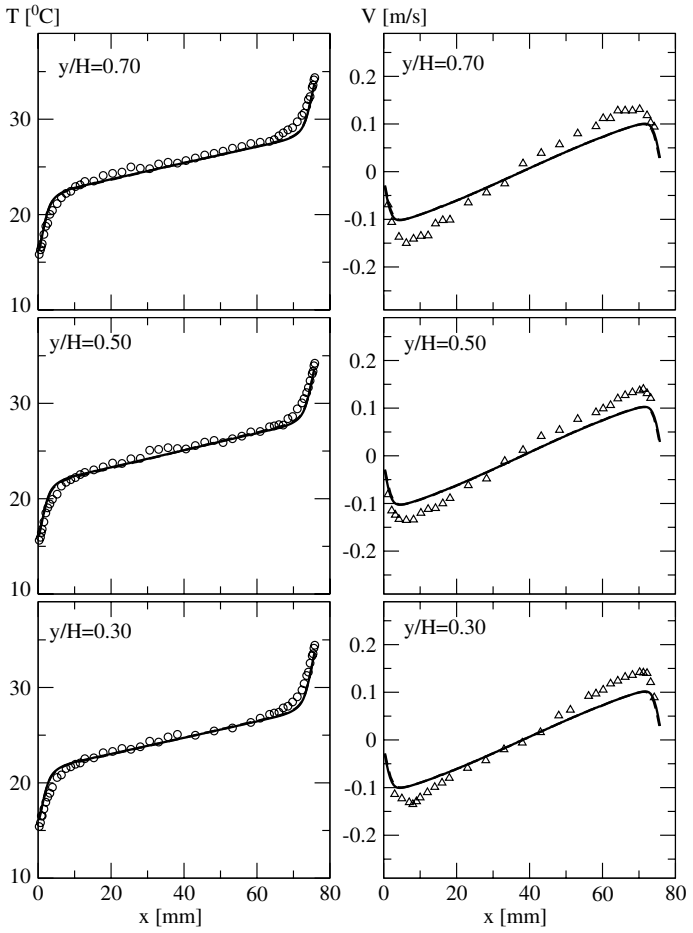

Fig. 8. Mean temperature and velocity profiles at various heights for the $Ra = 0.86 \times 10^6$ case.

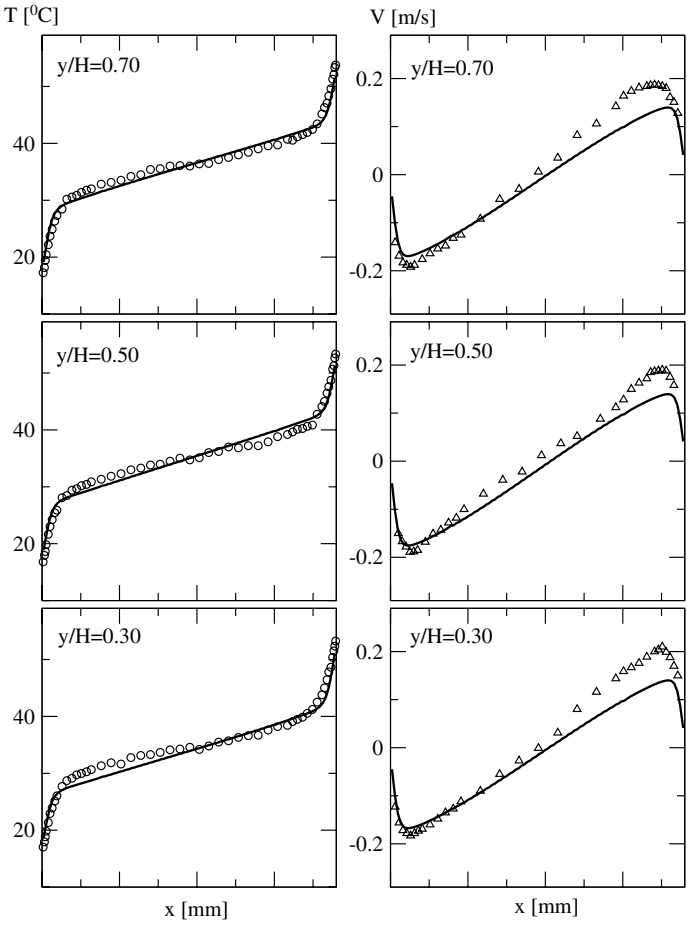

Fig. 9. Mean temperature and velocity profiles at various heights for the $Ra = 1.43 \times 10^6$ case.

turbulent flow/heat transfer modeling capability in this code.

4. Conclusions

The buoyancy model implemented here has been demonstrated to correctly and accurately represent the physics of buoyancy-driven flows. It captures the (in)stability of Rayleigh–Bénard convection near the critical Rayleigh number. It also accurately predicts the experimentally observed temperature and velocity fields in turbulent natural convection in a large aspect ratio enclosed cavity, for which no previous CFD work has been published per our best knowledge. As this code naturally inherits a number of attractive features, such as easy handling of complex geometry, fully parallel computation, and turbulence modeling capability, it should be suitable for a wide range of flow simulations involving buoyancy force.

The success of LBM in predicting buoyancy-driven flows is based on several physics and algorithmic advancements achieved in recent years. The addition of capability to simulate natural convection should help LBM to become a more powerful tool amongst engineers and researchers in the CFD community and in return will help us better understand and further improve the lattice Boltzmann method.

Acknowledgements

This work has been partially supported by the NSF Grant DMI 0239176. The authors are grateful to Charles Alexander, Olga Fillippova, Satheesh Kandasamy, Alexander Konstantinov, Richard Shock, and Victor Yakhot for their contributions to validation and development of the baseline hybrid LBM/macroscopic approach for turbulent heat transfer that lays foundation for the buoyancy code used here.

References

[1] A. Bejan, Convection Heat Transfer, Wiley, New York, 1984.

[2] W. Cabot, P. Moin, Approximate wall boundary conditions in the large-eddy simulation of high reynolds number flow, Flow, Turbulence Combust. 63 (1999) 269–291.

[3] A. Juneja, J.G. Brasseur, Characteristics of subgrid-resolved-scale dynamics in anisotropic turbulence, with application to rough-wall boundary layers, Phys. Fluids 11 (1999) 3054–3068.

[4] Y. Zhou, J.G. Brasseur, A. Juneja, A resolvable subfilter-scale model specific to large-eddy simulation of under-resolved turbulence, Phys. Fluids 13 (2001) 2602–2610.

[5] F. Massaioli, R. Benzi, S. Succi, Exponential tails in 2-dimensional Rayleigh–Benard convection, Europhys. Lett. 21 (3) (1993) 305.

[6] A. Bartoloni, C. Battista, S. Cabasino, P.S. Paolucci, et al., LBE simulations of Rayleigh–Benard convection on the APE100 parallel processor, Int. J. Mod. Phys. C 4 (1993) 993–1006.

[7] R. Benzi, R. Tripiccione, F. Massaioli, S. Succi, S. Ciliberto, On the scaling of the velocity and temperature structure functions in Rayleigh–Benard convection, Europhys. Lett. 25 (1994) 341.

[8] X. Shan, Simulation of Rayleigh–Bénard convection using a lattice Boltzmann method, Phys. Rev. E 55 (1997) 2780–2788.

[9] R. Benzi, S. Succi, M. Vergassola, The lattice-Boltzmann equation — theory and applications, Phys. Rep. 222 (1992) 145.

[10] S. Chen, G. Doolen, Lattice Boltzmann method for fluid flows, Ann. Rev. Fluid Mech. 30 (1998) 329–364.

[11] F. Higuerai, J. Jimenez, Boltzmann approach to lattice gas simulations, Europhys. Lett. 9 (1989) 663.

[12] F. Higuera, S. Succi, R. Benzi, Lattice gas dynamics with enhanced collisions, Europhys. Lett. 9 (4) (1989) 345–349.

[13] H. Chen, S. Chen, W. Matthaeus, Recovery of the Navier–Stokes equations using a lattice-gas Boltzmann method, Phys. Rev. A 45 (8) (1992) 5339–5342.

[14] Y. Qian, D. d'Humieres, P. Lallemand, Lattice BGK models for Navier–Stokes equation, Europhys. Lett. 17 (1992) 479–484.

[15] H. Chen, C. Teixeira, K. Molvig, Digital physics approach to computational fluid dynamics, some basic theoretical features, Int. J. Mod. Phys. C 8 (4) (1997) 675.

[16] S. Succi, H. Chen, C. Teixeira, G. Bella, A. De Maio, K. Molvig, An integer lattice realization of a lax scheme for transport processes in multiple component fluid flows, J. Comp. Phys. 152 (2) (1999) 493–516.

[17] H. Chen, S. Kandasamy, S. Orszag, R. Shock, S. Succi, V. Yakhot, Extended Boltzmann kinetic equation for turbulent flows, Science 301 (2003) 633–636.

[18] V. Yakhot, S. Orszag, S. Thangam, T. Gatski, C. Speziale, Development of turbulence models for shear flows by a double expansion technique, Phys. Fluids A 4 (7) (1992) 1510–1520.

[19] V. Yakhot, S. Orszag, J. Sci. Comp. 1 (1986) 3.

[20] M. Pervaiz, C. Teixeira, Two equation turbulence modeling in the context of lattice Boltzmann method, in: Proceedings of ASME PVP Conference of the Second International Symposium on Computational Technics for Fluid/Thermal/Chemical Systems with Industrial Applications, August 1–5, 1999, Boston, MA.

[21] C. Teixeira, Incorporating turbulence models into the lattice Boltzmann method, Int. J. Mod. Phys. C 9 (8) (1998) 1159.

[22] H. Chen, H-theorem and generalized semi-detailed balance condition for lattice gas systems, J. Statis. Phys. 81 (1995) 347–359.

[23] R. Zhang, H. Chen, Lattice Boltzmann method for simulations of liquid–vapor thermal flows, Phys. Rev. E 67 (6) (2003), Art. no. 066711 Part 2.

[24] H. Chen, C. Teixeira, K. Molvig, Realization of fluid boundary conditions via discrete Boltzmann dynamics, Int. J. Mod. Phys. C 9 (8) (1998) 1281.

[25] C. Alexander, H. Chen, S. Kandasamy, R. Shock, S.R. Govindappa, Simulations of engineering thermal turbulent flows using a lattice Boltzmann based algorithm, ASME PVP 424-1 (2001).

[26] R. Shock, S. Mallick, H. Chen, V. Yakhot, R. Zhang, Recent simulation results on 2D NACA airfoils using a lattice Boltzmann based algorithm, AIAA J. Aircraft 39 (3) (2002).

[27] R. Lietz, S. Mallick, S. Kandasamy, H. Chen, Exterior airflow simulations using a lattice Bolzmann approach, SAE, No. 2002-0154, 2000.

[28] X. He, S. Chen, G.D. Doolen, A novel thermal model for the lattice Boltzmann method in incompressible limit, J. Comput. Phys. 146 (1998) 282–300.

[29] S. Chen, H. Chen, D. Martinez, W. Matthaeus, Lattice Boltzmann model for simulation of magnetohydrodynamics, Phys. Rev. Lett. 67 (27) (1991) 3776–3779.

[30] U. Frisch et al., Lattice gas hydrodynamics in two and three dimensions, Complex Syst. 1 (1987) 649–707.

[31] F. Alexander, S. Chen, J. Sterling, Lattice Boltzmann thermohydrodynamics, Phys. Rev. E 47 (1993) 2249.

[32] H. Chen, C. Teixeira, H-theorem and origins of instability in thermal lattice Boltzmann models, Comp. Phys. Commun. 129 (2000) 21–31.

[33] N. Martys, H. Chen, Simulation of multicomponent fluids in complex three-dimensional geometries by the lattice Boltzmann method, Phys. Rev. E 53 (1) (1996) 743–750.

[34] H.S. Dol, K. Hanjalic, Computational study of turbulent natural convection in a side-heated near-cubic enclosure at a high Rayleigh number, Int. J. Heat Mass Transfer 44 (2001) 2323–2344.

[35] S.H. Peng, L. Davidson, Large eddy simulation for turbulent buoyant flow in a confined cavity, Int. J. Heat Fluid Flow 22 (2001) 323–331.

[36] P.L. Betts, I.H. Bokhari, Experiments on turbulent natural convection in an enclosed tall cavity, Int. J. Heat Fluid Flow 21 (2000) 675–683.

[37] R. Cheesewright, K.J. King, S. Ziai, Experimental data for the validation of computer codes for the prediction of two-dimensional buoyant cavity flows, in: ASME Winter Annual Meeting, HTD 60, 1986, pp. 75–81.

[38] A.A. Dafa'Alla, P.L. Betts, Experimental study of turbulent natural convection in a tall air cavity, Exp. Heat Transfer 9 (1996) 165–194.